Journal of Materials Chemistry A

ROYAL SOCIETY OF CHEMISTRY

PAPER

View Article Online
View Journal | View Issue

Cite this: J. Mater. Chem. A, 2024, 12, 10137

Interfacial polymerization of PEDOT sheath on V_2O_5 nanowires for stable aqueous zinc ion storage†

Ting Yang,§ Diheng Xin,§ Nan Zhang, Jing Li, Xianchi Zhang, Liqin Dang, Qi Li, Jie Sun, Xuexia He, Ruibin Jiang, Zonghuai Liu and Zhibin Lei ‡*

V_2O_5 is one of the promising cathodes for aqueous zinc ion batteries. However, its performance is largely hindered by its low conductivity and poor cycling stability due to the electrode dissolution. In this work, an interfacial polymerization strategy is developed to prepare the V_2O_5@poly(3,4-ethylenedioxythiophene) (PEDOT) core-sheath nanowire electrode. The interfacial redox reactions between the vapor 3,4-ethylenedioxythiophene molecules and V_2O_5 nanowires initiate the polymerization reaction to yield uniform PEDOT sheaths with varying thickness controlled by the reaction duration. The PEDOT sheaths are found to improve the electrode conductivity, suppress the V_2O_5 nanowire dissolution, and improve the specific capacity. Theoretical simulation further shows that the PEDOT sheath weakens the interactions between Zn^{2+} and the V_2O_5 host, thus benefiting the extraction of Zn^{2+} from the host electrode and boosting the cycling stability. Consequently, V_2O_5@PEDOT-50m delivers a specific capacity of 293 mA h g^{-1} at 0.1 A g^{-1} and 225 mA h g^{-1} at 1 A g^{-1}, which are superior to 205 mA h g^{-1} and 142 mA h g^{-1} of the pristine V_2O_5 nanowire electrode, respectively. Moreover, V_2O_5@PEDOT-50m maintains 97.8% and 99% capacity retention after 100 and 2000 cycles, respectively. The significantly enhanced performances with respect to the corresponding V_2O_5 nanowire counterpart demonstrate that the PEDOT sheaths developed by the interfacial polymerization could become an effective method to stabilize the vanadate-based cathodes for zinc ion storage.

Received 19th February 2024
Accepted 20th March 2024

DOI: 10.1039/d4ta01136h

rsc.li/materials-a

1. Introduction

The exploration of renewable and advanced sustainable energy storage devices is considered a potential route to resolve the ever-increasing fossil fuel consumption and environmental crisis. Lithium-ion batteries (LIBs) and supercapacitors are two representative energy storage devices that have received much attention during the past decades.[1] However, the low energy density of supercapacitors hinders their widespread applications in portable electronics and electric vehicles. While the LIBs have been widely used as the predominate power supply for various portable electronics due to their high energy density, long service life, and mature manufacturing technology,[2] the limited lithium resources, high manufacturing cost, and the potential safety risk arising from the use of flammable organic electrolytes have become the main concerns restricting their application in future grid-scale energy storage.[3]

Rechargeable aqueous zinc ion batteries (ZIBs) hold great potential for grid-scale energy storage by virtue of the large theoretical capacity (820 mA h g^{-1}), suitable redox potential (−0.763 V *vs.* SHE), and high volume capacity (5855 mA h cm^{-1}) of the metal zinc.[4–6] The use of an aqueous electrolyte can significantly reduce the safety risk and simultaneously improve the rate capability of aqueous ZIBs due to the fact that their ion conductivity is several orders of magnitude higher than that of an organic electrolyte.[7] Moreover, the abundant zinc resources, simple manufacturing technique, and low-toxicity aqueous electrolyte make the ZIBs a highly competitive energy storage device. However, the practical application of ZIBs is primarily hindered by the dissolution and poor stability of cathodes,

Key Laboratory of Applied Surface and Colloid Chemistry, MOE, Shaanxi Engineering Lab for Advanced Energy Technology, Shaanxi Key Laboratory for Advanced Energy Devices, School of Materials Science and Engineering, Shaanxi Normal University, 620 West Chang'an Street, Xi'an, Shaanxi, 710119, China. E-mail: zblei@snnu.edu.cn; Fax: +86-29-81530702; Tel: +86-29-81530810

† Electronic supplementary information (ESI) available: Schematic diagram showing the preparation of V_2O_5@PEDOT nanowires, SEM images of V_2O_5 and the V_2O_5@PEDOT aerogel, elemental composition, GCD curves of the V_2O_5 nanowire and PEDOT nanowire at 0.1 and 0.5 A g^{-1}, EIS spectra, GCD curves of the V_2O_5 nanowire at various current densities, cycling performance of V_2O_5@PEDOT, performance comparisons of the V_2O_5@PEDOT-50m nanowires electrode with previous cathodes, CV curves of the V_2O_5 nanowires and the corresponding curves of log(*i*) *vs.* log(*v*), *ex situ* XRD patterns of the V_2O_5@PEDOT-50m electrode in the second cycle. See DOI: https://doi.org/10.1039/d4ta01136h

§ Ting Yang and Diheng Xin contributed equally to this work.

‡ Prof. Zhibin Lei, School of Materials Science and Engineering, Shaanxi Normal University, 199 South Chang'an Road, Xi'an, Shaanxi, 710062, China.

dendrite growth, and side reactions of the Zn anode sides.[8,9] In particular, the exploration of stable cathodes with high specific capacity and long cycling life remains a challenge for the future practical application of ZIBs.

So far, manganese-based oxides,[10,11] Prussian blue analogues[12,13] and vanadium based compounds[14–18] have been extensively investigated as potential cathodes for ZIBs. Among them, the vanadium oxides have attracted much interest due to their multiple redox reactions and layered or tunnel structure.[19–21] V_2O_5 is a layered structure in which each layer is built by the edge and corner-sharing VO_5 pyramid, and can offer a theoretical capacity of 589 mA h g^{-1} based on the two-electron redox reaction.[5] Despite these structural advantages, the V_2O_5 cathodes face capacity decay due to electrode dissolution and structural collapse during the repeated charging and discharging process. To resolve these issues, pre-insertion of cations,[14,22,23] metal ion doping,[24] intercalation of H_2O molecules[25] or two-dimensional materials[18,26] have been reported to stabilize the V_2O_5 cathodes. In spite of the improved performances, some issues still exist, including decreased valence state of V, reduced active sites and increased interactions between the pre-inserted cations and oxide layers of the host cathode.[26] On the other hand, the intrinsic low conductivity of V_2O_5 (10^{-3}–10^{-4} S cm^{-1})[7,27] is inadequate for high-rate applications. Consequently, the conductive $Ti_3C_2T_x$ MXene layer or SWCNT are assembled with vanadium oxides to enhance the electrode conductivity and suppress the vanadium dissolution.[28,29] Alternatively, the conductive polymers poly(3,4-ethylenedioxythiophene) (PEDOT)[30,31] are also attractive for stabilizing V_2O_5-based cathodes.[32,33] For instance, the small molecules PEDOT were inserted into V_2O_5 nanoflakes to improve the electrode conductivity and facilitate the Zn^{2+} diffusion kinetics.[30] In another work by Cao *et al.*,[32] polymerization of PEDOT layers on the sodium vanadate nanobelts ($Na_{0.76}V_6O_{15}$) was found to produce oxygen vacancies, which offers a large interplanar distance, enhances electron transfer and benefits Zn^{2+} diffusion. However, the PEDOT layers with controllable thickness still remain a great challenge for high-efficiency Zn^{2+} storage. Moreover, the effects of the PEDOT layer thickness on the reaction kinetics have rarely been investigated.

In this work, a facile interfacial polymerization reaction between vapor 3, 4-vinyl dioxthiophene (EDOT) and V_2O_5 nanowires is reported to prepare the V_2O_5@PEDOT core-sheath electrode. The redox reactions at the EDOT/V_2O_5 interfaces yield uniform PEDOT sheaths with thickness varying from 23 to 43 nm by extending the polymerization durations. The PEDOT sheaths are proven to enhance the nanowire conductivity, weaken the interactions between the Zn^{2+} ions and V_2O_5 host layers, and suppress the electrode dissolution. As a consequence, the V_2O_5@PEDOT nanowires exhibit dramatically enhanced performances in term of the specific capacity, long-term cyclability and rate performance, making the interfacial polymerization a facile yet effective solution to stabilize vanadium-based cathodes for future grid-scale zinc ion storage.

2. Results and discussion

The fabrication procedure of the V_2O_5@PEDOT core-sheath nanowires is schematically illustrated in Fig. S1a.† Firstly, the V_2O_5 nanowire suspensions prepared by a hydrothermal synthesis[33] were transferred into a PTFE mold, followed by freeze-drying to form the V_2O_5 sponge (Fig. S2a†). It is noted that such highly porous sponge allows sufficient contact of the gaseous EDOT molecules with the nanowires. As the temperature increases to 80 °C, the EDOT liquid starts to evaporate into gaseous molecules and react with V_2O_5 nanowires, which serves as a good oxidant to initiate the polymerization reaction at the EDOT/V_2O_5 nanowire interfaces (Fig. 1). Consequently, PEDOT sheaths of different thicknesses can be readily formed by adjusting the reaction time. As indicated by the optical photographs of the V_2O_5 sponge in Fig. 2a, the product gradually evolves from a light yellow color to dark green with the increase of the reaction time from 20 to 60 min. Such changes mean that more PEDOT has been coated on the nanowires to form the V_2O_5 core and PEDOT sheath. In spite of different sheath thicknesses of PEDOT, all of the V_2O_5@PEDOT remain sponge-like structures resembling that of the pristine V_2O_5 (Fig. S2a–f†). Fig. 2b–g shows the magnified SEM images of individual V_2O_5 and the V_2O_5@PEDOT nanowires in the corresponding sponge. No noticeable phase separations are observed, except the reaction time reaching 60 min. At this state, polymerization of EDOT molecules occurs between V_2O_5 nanowires, yielding the V_2O_5@PEDOT composite electrode with PEDOT fibers connecting V_2O_5 nanowires (Fig. 2g).

The phase structures of the V_2O_5@PEDOT products were identified by XRD and Raman spectroscopy (Fig. 2h–j). The V_2O_5 nanowires exhibit sharp diffraction peaks at 15.3°, 20.2°, 21.7° and 31.0°, which can be indexed to the (200), (001), (101) and (301) diffraction planes of orthorhombic V_2O_5 (JCPDS no 41-1426),[34,35] respectively, and suggests high purity and good crystallinity of the nanowires. In contrast, the V_2O_5@PEDOT samples exhibit XRD patterns similar to those of the pristine V_2O_5, except that all of the intensities are slightly reduced. A plausible reason for such changes is due to the scarified V_2O_5 nanowires, which react with EDOT molecules and yield the low crystallinity of V_2O_5@PEDOT. The Raman spectroscopy of pristine V_2O_5 and V_2O_5@PEDOT nanowires are illustrated in Fig. 2i and j, respectively. In the low-frequency region, the intense peak at around 139 cm^{-1} is attributed to the skeleton bending vibration of the V–O–V bond. The peaks at 286 and 408 cm^{-1} correspond to the bending vibrations of O_3–V═O and V–O_3–V, respectively.[18] The distinct peak at 993 cm^{-1} is ascribed to the in-phase stretching vibration mode of the apical V═O bond.[36,37] According to Fig. 2i, the Raman peaks of V_2O_5@-PEDOT do not show noticeable changes in both position and intensity after PEDOT coating. In the high-frequency region (Fig. 2j), Raman bands at around 1359, 1437, 1492 and 1573 cm^{-1} are attributed to the symmetric and asymmetric tensile vibrations of C_α and C_β in PEDOT.[38,39] However, unlike the profiles of V_2O_5@PEDOT in the low-frequency region, these peaks in the high-frequency region gradually increase with the

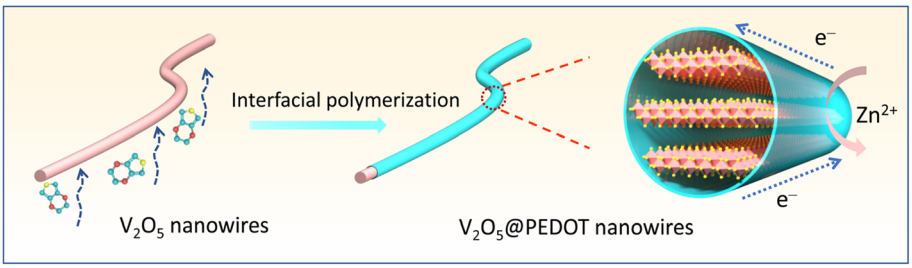

Fig. 1 Schematic showing the interfacial polymerization of the PEDOT sheath on the V_2O_5 nanowires.

polymerization duration, which are consistent with the optical images, and thus indicate that more PEDOT have been coated on the V_2O_5 nanowires at longer reaction times.

The uniform coating of PEDOT on the V_2O_5 nanowires are further confirmed by TEM characterization. Fig. 3a–f shows the TEM images of a single V_2O_5 and V_2O_5@PEDOT nanowire at different reaction times. Clearly, both V_2O_5 and V_2O_5@PEDOT nanowire display smooth surfaces without any PEDOT aggregates, which coincides with the SEM images and demonstrates the homogeneous PEDOT coating on each V_2O_5 nanowire. The uniform coating is further elucidated by the elemental mapping images, as displayed in the overlay (Fig. 3b1–3f1) and individual elemental mapping images (Fig. 3b2–3f2). In contrast to the V_2O_5 nanowire (Fig. 3a1 and 3a2), all V_2O_5@PEDOT samples display additional S and C elements, which are exclusively from the PEDOT molecules. The uniform distribution of both S and C elements outside the V_2O_5 nanowires reveals the effective interfacial polymerization reactions. Besides the uniform PEDOT sheaths, their thicknesses could also be facilely adjusted by simply controlling the interfacial polymerization

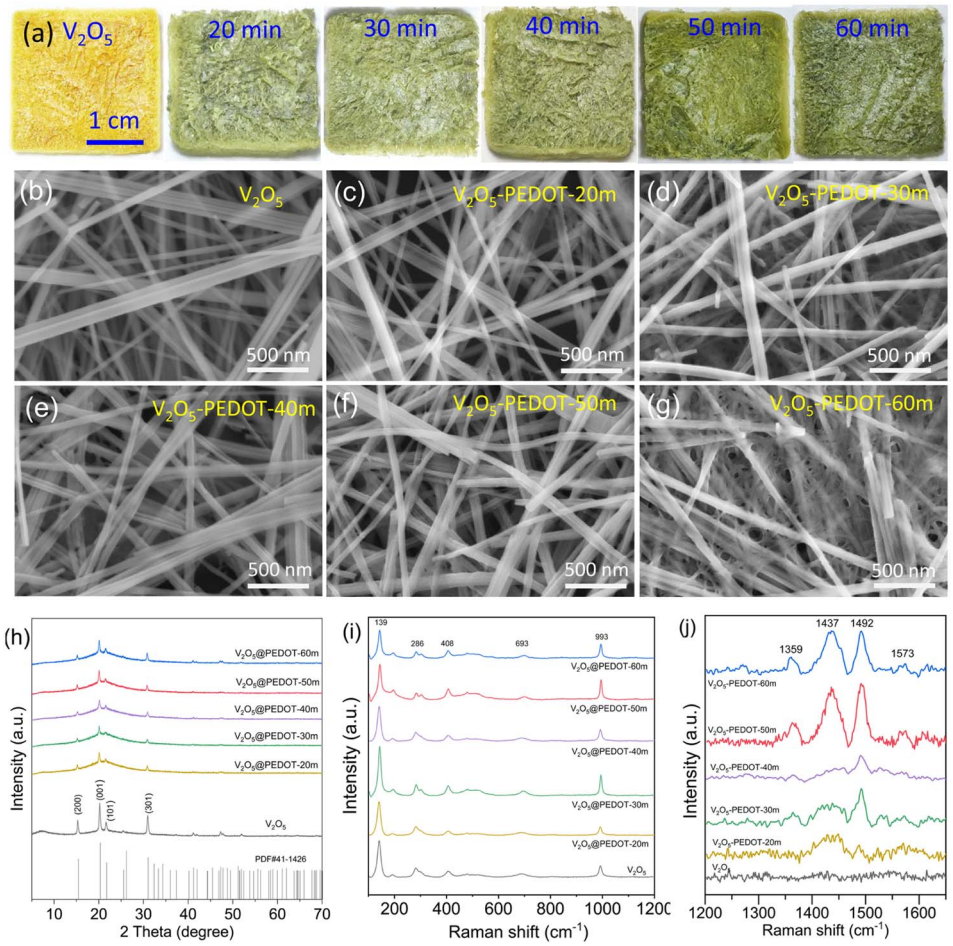

Fig. 2 Digital photographs (a), SEM images (b–g), XRD patterns (h), Raman spectra in the low (i) and high frequency (j) regions of the aerogels composed of V_2O_5 nanowires and V_2O_5@PEDOT nanowires.

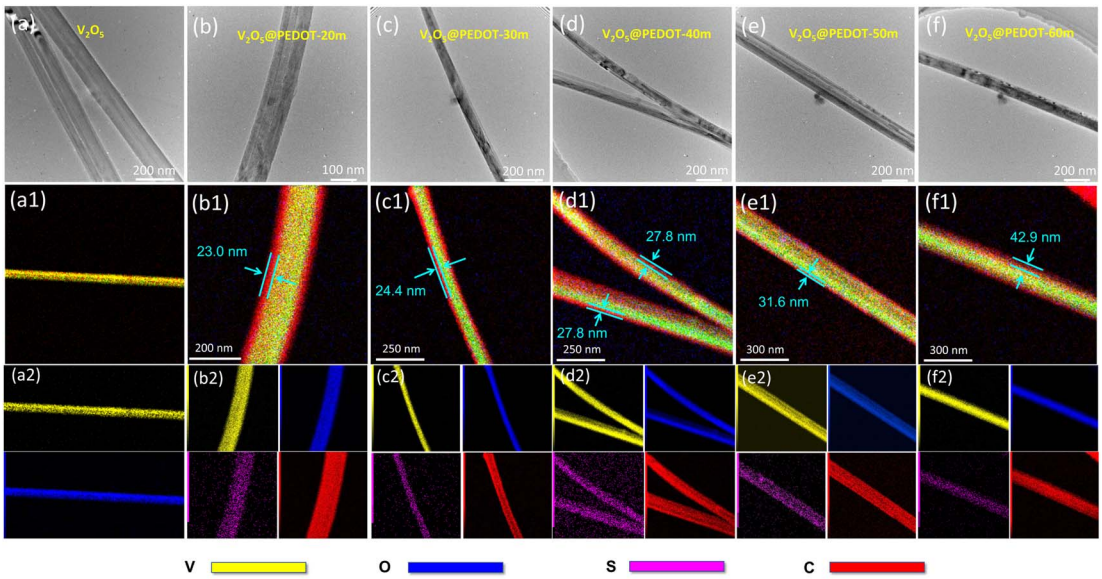

Fig. 3 TEM images (a–f), the corresponding overlay elemental mapping images (a1–f1), and the V, O, S, C elemental mapping images (a2–f2) of the V_2O_5 nanowires and V_2O_5@PEDOT nanowires.

durations. On the basis of the overlay elemental mapping (Fig. 3b1–3f1), the PEDOT sheath thickness can be roughly determined, which are plotted in Fig. 4a. The results showed that extending the polymerization time from 20 to 60 min leads to the thickness increase of the PEDOT sheath from 23 to 43 nm. Importantly, such PEDOT sheaths could enhance the

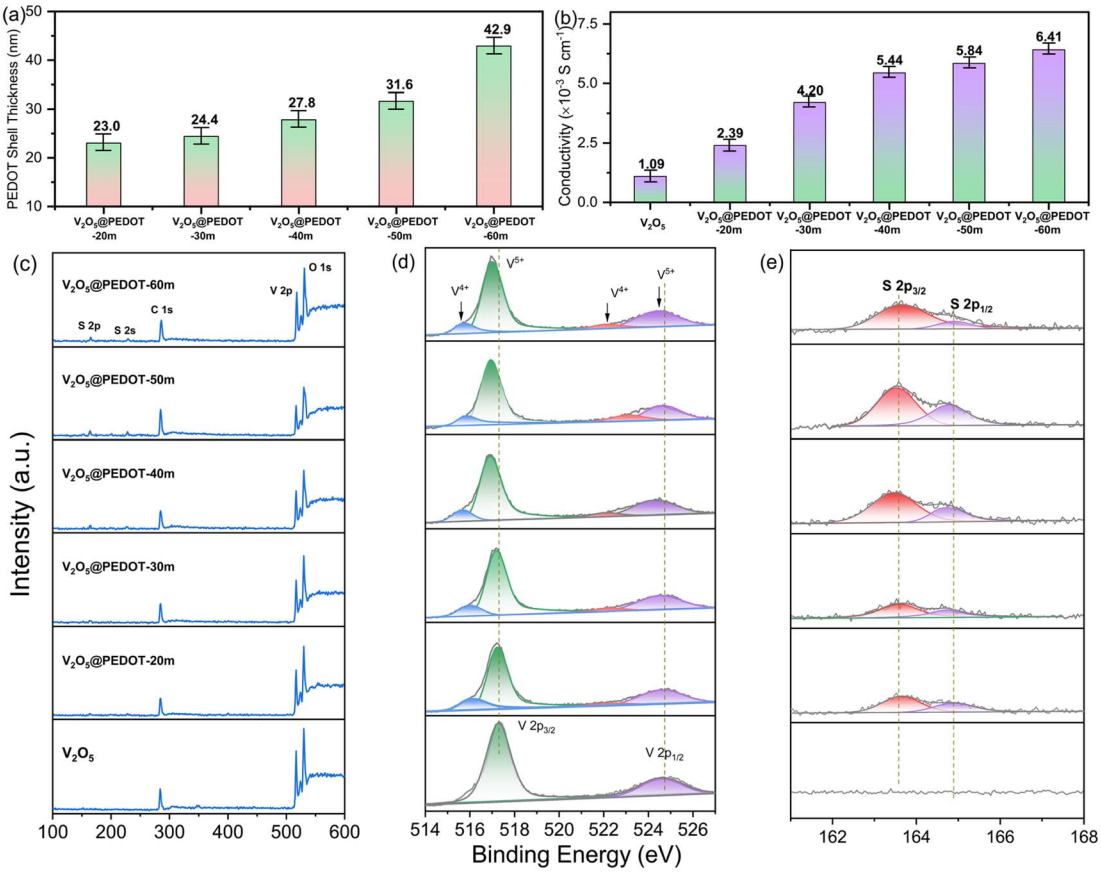

Fig. 4 PEDOT sheath thickness (a), the conductivity (b), survey XPS spectra (c), V 2p XPS spectra (d) and S 2p XPS spectra (e) of the V_2O_5 and V_2O_5@PEDOT nanowires.

overall conductivity of the V_2O_5@PEDOT electrodes. As depicted in Fig. 4b, the V_2O_5@PEDOT-30 m exhibits a conductivity that is 4-fold higher (4.2×10^{-3} S cm^{-1}) as compared with pristine V_2O_5 nanowires (1.09×10^{-3} S cm^{-1}). When the reaction time is over 40 min, the conductivity of V_2O_5@PEDOT reaches an approximate plateau of $\sim 6 \times 10^{-3}$ S cm^{-1}.

The XPS characterization was carried out to determine the valence states of the V_2O_5 nanowire at different polymerization durations (Fig. 4c–e). Besides the peaks at 536 and 516 eV corresponding to the O 1s and V 2p (Fig. 4c), respectively, the survey XPS spectra of the V_2O_5@PEDOT nanowires exhibit additional S weak signals at ~164 eV, confirming the coexistence of V_2O_5 and PEDOT in the V_2O_5@PEDOT nanowires. The high-resolution XPS spectrum of the V_2O_5 nanowires exhibits a strong peak at 517.3 eV and a weak peak at 524.5 eV (Fig. 4d). These peaks correspond to the spin–orbit splitting of V $2p_{3/2}$ and V $2p_{1/2}$, respectively, and suggest a V^{5+} chemical valence in the V_2O_5 nanowires.[14] As the interfacial polymerization reactions proceed, these two peaks shift toward low binding energy. More importantly, accompanied with the downshift of these peaks, two additional peaks at 516.2 and 523.0 eV are observed for all of the V_2O_5@PEDOT samples. These weak peaks are ascribed to V^{4+}.[40] The reduction of partial V^{5+} into V^{4+} by EDOT molecules induces the uniform PEDOT sheaths, which are further confirmed by the S 2p XPS spectra. As displayed in Fig. 4e, two peaks of S $2p_{3/2}$ (163.7 eV) and S $2p_{1/2}$ (165.1 eV) stem from the thiophene in PEDOT molecules.[38] By integrating the peak areas of V^{4+} to the total V peak areas, the amount of V^{4+} in the V_2O_5@PEDOT was calculated in Table S1.† The ratio of the V^{4+}/V increases with the polymerization time, and reaches a maximal value of 16.5% for V_2O_5@PEDOT-50m. Such changes decrease the average valence state of V from +5.0 of the initial V_2O_5 nanowires to +4.85 of V_2O_5@PEDOT-60m (Table S1†). Moreover, due to the formation of the PEDOT sheath, the contents of the surface sulfur increase, while that of the surface vanadium decreases accordingly. The above observations coincide well with the thickness of PEDOT sheaths, and thus demonstrate that the structure of V_2O_5@PEDOT nanowires can be facilely controlled by adjusting the interfacial oxidation polymerization time.

The electrochemical properties of the V_2O_5@PEDOT nanowires as cathodes for zinc ion storage were assessed by assembling a series of coin-type cells with zinc foil as the anode and 2.0 M $Zn(CF_3SO_3)_2$ as the aqueous electrolyte. Fig. 5a and Fig. S3† show the galvanostatic charge discharge profiles of the V_2O_5@PEDOT nanowires at 0.1 and 0.5 A g^{-1}, respectively. Clearly, two discharge potential plateaus in the range of 1.01–0.81 V and 0.64–0.40 V (*vs.* Zn^{2+}/Zn) are evidenced, which are attributed to the insertion of Zn^{2+} into the V_2O_5@PEDOT nanowires. Fig. 5b compares the discharge capacity of V_2O_5@PEDOT at a current density of 0.1 and 1.0 A g^{-1}. Specifically, the V_2O_5@PEDOT-50m electrode exhibits discharge capacities of 293 and 225 mA h g^{-1} at 0.1 and 1.0 A g^{-1}, respectively, which are much higher than that of the V_2O_5 nanowires (205 and 142 mA h g^{-1}) and PEDOT nanowires electrode (68 and 58 mA h g^{-1}) at the same current density (Fig. S4†). It is noted that the capacity of the V_2O_5@PEDOT-50m is much higher than those of the cationic intercalated vanadium oxide cathodes, which are usually below 200 mA h g^{-1}.[17] The Nyquist plots of the V_2O_5 and V_2O_5@PEDOT-50m nanowires electrodes are compared in Fig. S5.† Clearly, the V_2O_5@PEDOT-50m electrode exhibits significantly reduced charge transfer resistance, which is closely related to the conductive PEDOT sheath coating. The enhanced conductivity affords V_2O_5@PEDOT-50m with high rate capability. The average discharge capacities decrease from 293 to 224, 169, 136 and 110 mA h g^{-1} upon the increase of the current density from 0.1 to 0.5, 1.0, 2.0 and 5.0 A g^{-1}, respectively (Fig. 5c). Importantly, even with the 50-fold current increase from 0.1 to 5.0 A g^{-1}, the electrode is still capable of retaining 37.5% capacity (110 mA h g^{-1}) with respect to the initial capacity of 293 mA h g^{-1} at 0.1 A g^{-1} (Fig. 5d). In contrast, only 29.0% capacity can be maintained for the V_2O_5 nanowires electrode under the identical testing condition (Fig. 5d and S6†). Moreover, the V_2O_5@PEDOT-50m electrode could resume 62% of its initial capacity when returning the current density to initial 0.1 A g^{-1} after 90 cycles. On the basis of these results, the larger capacity and enhanced rate capacity of the V_2O_5@PEDOT-50m electrode are attributed to the uniform PEDOT sheaths, which not only improve the electrode conductivity, but also boost the electrode electrochemical durability.

Apart from the enhanced capacity and rate capability, PEDOT sheaths also significantly boost the cycling performances of the V_2O_5@PEDOT electrode. In spite of different PEDOT sheath thicknesses, the V_2O_5@PEDOT electrodes exhibit overall enhanced cycling stability with respect to the V_2O_5 nanowire electrodes at 1.0 A g^{-1} (Fig. S7†). Taking V_2O_5@PEDOT-30m as example, a capacity retention of 82.6% relative to the 32.1% of the V_2O_5 nanowires has been achieved. Fig. 5e and S8† show the long-term durability of the V_2O_5@PEDOT-50m electrode at 0.1 A g^{-1} and 10 A g^{-1}, respectively. After continuous cycling at 0.1 A g^{-1} for 100 cycles, the V_2O_5@PEDOT-50m electrode exhibits a discharge capacity of 265 mA h g^{-1}, and a capacity retention of 97.8% with respect to its first discharge capacity of 271 mA h g^{-1} (Fig. 5e). Conversely, although the V_2O_5 nanowires electrode has an initial discharge capacity of 206 mA h g^{-1}, it decays rapidly to 52.5 mA h g^{-1} after 100 cycles at 0.1 A g^{-1} (25.5% capacity retention). In the meantime, at a high current density of 10 A g^{-1}, an initial discharge capacity of 89 mA h g^{-1} and a capacity maintenance of 99% (88.2 mA h g^{-1}) have been achieved for the V_2O_5@PEDOT-50m electrode after 2000 cycles (Fig. S8†). These performances are superior to the counterpart V_2O_5 nanowires with a low initial capacity of 51.8 mA h g^{-1} and a poor capacity maintenance of 41.8%. Table S2† summarizes the performance of vanadium and manganese-based cathodes. While the V_2O_5@PEDOT-50m displays relatively low specific capacity as compared with the $V_2O_5 \cdot nH_2O$/graphene,[25] porous V_2O_5 microspheres[41] or 3D@V_2O_5,[42] its cycling stability is remarkably improved as compared with V_2O_5, cationic intercalated vanadium oxides,[43,44] and some MnO_2-based cathodes[10,45] (Table S2†). In addition to the above outstanding electrochemical stability, the V_2O_5@PEDOT-50m electrode exhibits nearly 100% coulombic efficiency at both low and high current densities, suggesting the superior reversibility of the Zn^{2+} insertion/

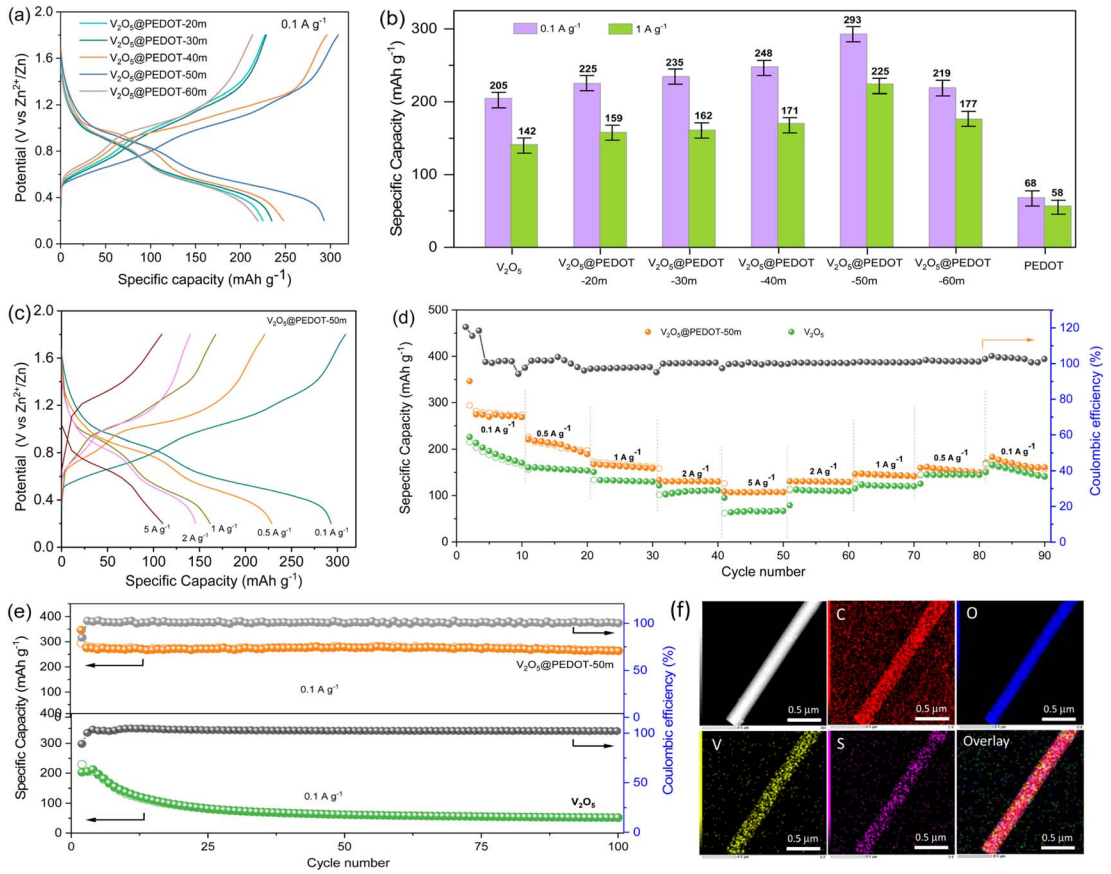

Fig. 5 CV curves of the V_2O_5@PEDOT electrodes at 0.1 A g^{-1}, the specific capacity of the V_2O_5@PEDOT electrodes at 0.1 and 1.0 A g^{-1} (b), the charge discharge profiles of V_2O_5@PEDOT-50m at various rates (c), rate capability of V_2O_5 and V_2O_5@PEDOT-50m (d), cycling performance of V_2O_5 and V_2O_5@PEDOT-50m at 0.1 A g^{-1} for 100 cycles (e), and the elemental mapping images of the cycled V_2O_5@PEDOT-50m (f).

extraction within this electrode. The elemental mapping images of the cycled V_2O_5@PEDOT-50m are shown in Fig. 5f. The core-sheath structure is well maintained even after continuous charging and discharging at 0.1 A g^{-1} for 100 cycles, further confirming the vital role of the PEDOT sheaths in protecting the structural integrity of the V_2O_5@PEDOT-50m electrode.

It is known that the strong electrostatic interactions between the Zn^{2+} and V_2O_5 host could trap a certain amount of Zn^{2+},[9] leading to the unsatisfying electrochemical reversibility and poor cycling performances. In order to explore the impact of the PEDOT sheaths on this effect, density functional theory (DFT) was used to calculate the binding energy of the inserted Zn^{2+} with the V_2O_5 host. Our calculation model was established using the $V_2O_5 \cdot 1.5H_2O$ molecular formula. According to the aforementioned XPS quantitative analysis, the bulk phase of V_2O_5@PEDODT was composed of 83.3% V^{5+}, while the surface V^{4+} coated with PEDOT molecules was 16.7% (Fig. 6a). It is noteworthy that V^{4+} in the host V_2O_5 are more likely to combine with O from PEDOT to form the most stable V–O bonding (Fig. 6b). In this case, the binding energy of Zn^{2+} with V_2O_5@PEDOT is markedly reduced to −0.07 eV as compared with −2.29 eV of the pristine V_2O_5 nanowires electrode (Fig. 6c). Such weakened electrostatic interactions between Zn^{2+} and the V_2O_5 host suggest that most of the inserted Zn^{2+} can be reversibly extracted from V_2O_5@PEDOT. On the other hand, the impact of the PEDOT coating on the vanadium dissolution was also investigated by placing the active electrodes in 2 M aqueous $Zn(CF_3SO_3)_2$ electrolyte for different days. The dissolved vanadium in the electrolyte after 12 days is determined to be 9.2 mg L^{-1} for the V_2O_5@PEDOT-50m electrode, which is one-half lower than 17.7 mg L^{-1} of the V_2O_5 nanowires electrode (Fig. 6d). The remarkably reduced binding energy and the suppressed vanadium dissolution contribute to the enhanced cycling stability of V_2O_5@PEDOT-50m, as discussed in Fig. 5e and S8.†

The CV curves of V_2O_5@PEDOT-50m recorded at 0.1 mV s^{-1} in the potential range of 0.2–1.8 V is presented in Fig. 7a. For the V_2O_5@PEDOT-50m electrode, three prominent oxidation peaks at around 0.75, 1.05, 1.40 V and the corresponding reduction peaks at 0.46 and 0.78 V are evident, which can be ascribed to the redox couples of V^{5+}/V^{4+} and V^{4+}/V^{3+}, respectively.[46] As compared with the V_2O_5 nanowires electrode, the oxidation peaks of the V_2O_5@PEDOT-50 m electrode slightly shift towards high potential and their reduction peaks shift to low potential. Such polarization phenomenon is induced by the slow ion diffusion (discussed below). This phenomenon becomes more evident at higher scan rates (Fig. 7b), where an apparent ion concentration gradient would limit the redox reactions near the electrode.[7]

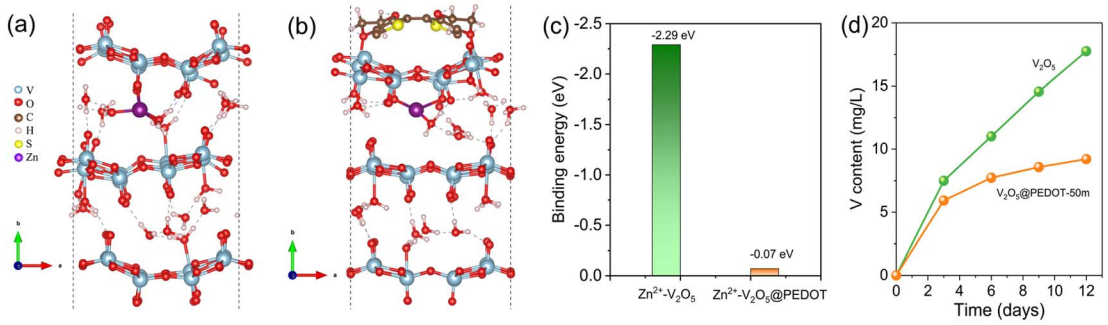

Fig. 6 The crystal structure of $V_2O_5 \cdot 1.5H_2O$ (a) and the possible V–O bonding mode (b) formed by V from host V_2O_5 and O in the PEDOT chain. The binding energy of Zn^{2+}-V_2O_5 and Zn^{2+}-V_2O_5@PEDOT (c), and the variation of the V concentration by placing the V_2O_5 and V_2O_5@PEDOT-50m electrodes in 2 M aqueous $Zn(CF_3SO_3)_2$ electrolyte for different days (d).

To understand the Zn^{2+} storage behaviors, the electrochemical kinetics were analyzed using the method developed by Dunn *et al.*[47]

$$i = av^b$$

In this equation, the adjustable coefficient parameter b can be utilized to distinguish the pseudocapacitive or diffusion-controlled electrochemical behavior.[23] Fig. 7c plots the CV curves of the V_2O_5@PEDOT-50m electrode of various scan rates. The linear fitting of $\log(i)$ *vs.* $\log(v)$ yields the b values of 0.53, 0.52, 0.59 and 0.55 for the four peaks, respectively. These values are close to 0.5 and suggest that the diffusion-controlled behaviors dominate the insertion/extraction of the Zn^{2+} ion into/from the V_2O_5@PEDOT-50m nanowires. Whereas, the V_2O_5 nanowires electrode presents a higher b value (Fig. S9†) under the identical condition. This comparison means that the

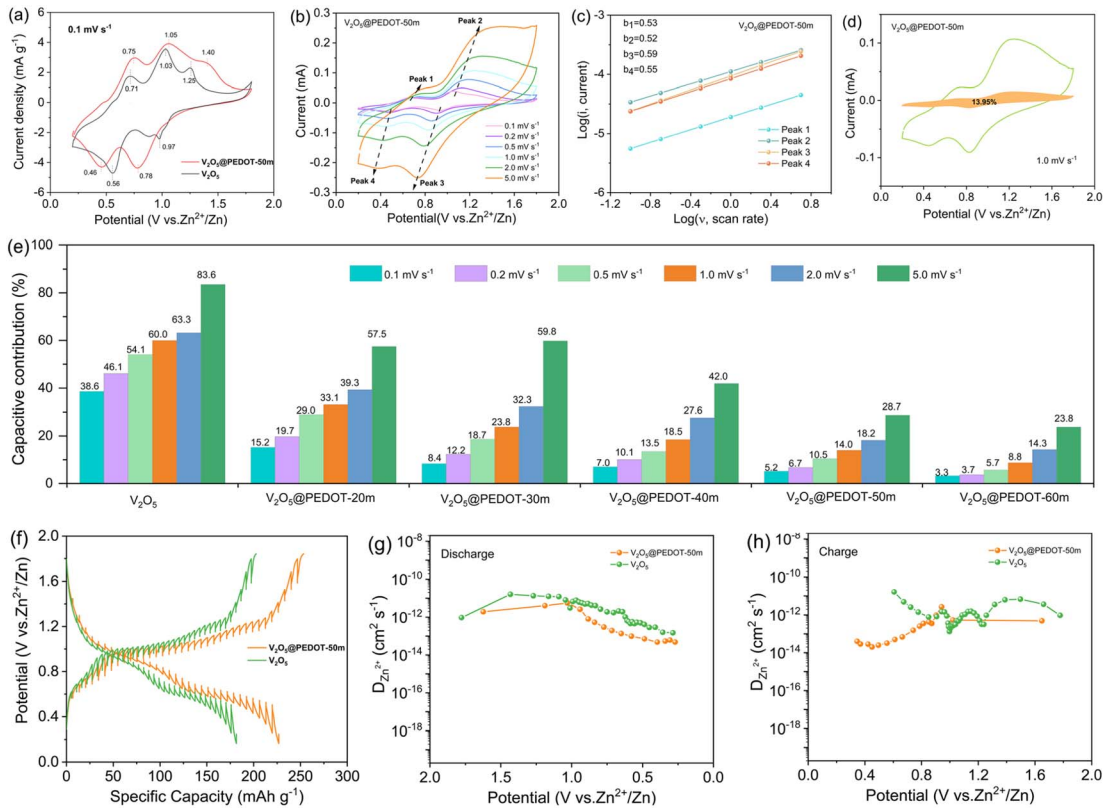

Fig. 7 CV curves of V_2O_5 and V_2O_5@PEDOT-50m at 0.1 mV s^{-1} (a), and CV curves of V_2O_5@PEDOT-50m at various scan rates (b). The linear fitting of the $\log(i)$ *vs.* $\log(v)$ (c), the CV curves of V_2O_5@PEDOT-50m at 1.0 mV s^{-1} with the shaded area showing the current contribution from the pseudocapacitance (d). The pseudocapacitive contribution from 0.1 to 5.0 mV s^{-1} for the V_2O_5 and V_2O_5@PEDOT electrodes at various scan rates. GITT profiles (f), and the calculated Zn^{2+} diffusion coefficient in the discharge (g) and charge (h) process for the V_2O_5 and V_2O_5@PEDOT-50m electrodes.

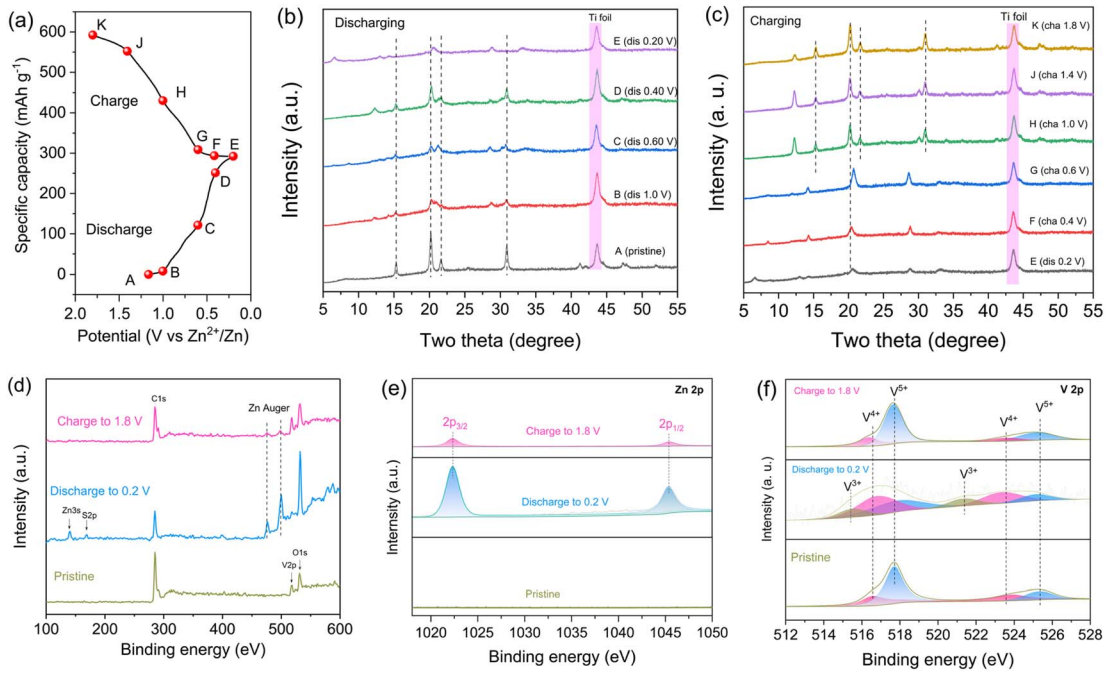

Fig. 8 The potential–capacity profile (a), the *ex situ* XRD patterns of V_2O_5@PEDOT-50m in different discharge (b) and charge states (c) of the first cycle. The survey XPS spectra (d), Zn 2p (e), and V 2p (f) XPS spectra (f) at different discharge and charge states.

protective PEDOT sheaths would decrease the Zn^{2+} ion kinetics by slowing the ion diffusion into the V_2O_5@PEDOT-50m electrode.

In order to quantitatively analyze the current contribution from the pseudocapacitive and diffusion-controlled electrochemical process, the following equation is adopted:[48,49]

$$i = k_1 v + k_2 v^{1/2} \quad (1)$$

where the total current (i) is regarded to be contributed from the pseudocapacitive ($k_1 v$) and the diffusion-controlled ($k_2 v^{1/2}$) process. Fig. 7d depicts the CV curves of V_2O_5@PEDOT-50m at 1.0 mV s^{-1}. As indicated by the shaded area, the current contribution from the pseudocapacitive process is about 14.0%, and this percentage gradually increases to 28.7% at scan rate of 5.0 mV s^{-1} (Fig. 7e). To further understand the effect of the PEDOT shell thickness on the reaction kinetics, pseudocapacitive contributions of various V_2O_5@PEDOT electrodes at different scan rates are plotted in Fig. 7e. It can be seen that for each electrode, the pseudocapacitive contributions always increase with the scan rates, which are consistent with the previous V_2O_5 cathodes.[35] However, at a given scan rate, the pseudocapacitive contributions of V_2O_5@PEDOT are lower than that of the pure V_2O_5 nanowires. Moreover, such pseudocapacitive contribution progressively decreases with the increase of the PEDOT sheath thickness. For example, at 0.1 mV s^{-1}, the capacitive contribution decreases from 38.6% of the V_2O_5 nanowires to 3.3% of V_2O_5@PEDOT-60m. These results indicate that the thicker PEDOT sheaths could block Zn^{2+} diffusion and lower the ion kinetics through spatial physical constraint. This conclusion is further supported by measuring the diffusion behaviors of Zn^{2+} through galvanostatic intermittent titration technique (GITT). Fig. 7f depicts the typical GITT profiles of the V_2O_5 and V_2O_5@PEDOT-50m electrodes in the second discharge/charge cycle at 0.1 A g^{-1}. The corresponding Zn^{2+} diffusion coefficients ($D_{Zn^{2+}}$) calculated from the GITT are displayed in Fig. 7g and h. In the discharge process, the calculated $D_{Zn^{2+}}$ values for the V_2O_5 nanowires stay in the magnitude range from 10^{-13} to 10^{-11} cm^2 s^{-1}, which are comparable to previous results of the V_2O_5 nanopaper[50] and Ba or Al-modified V_2O_5.[24,51] In contrast, the V_2O_5@PEDOT-50m presents a slightly smaller $D_{Zn^{2+}}$ in both charge and discharge processes. These observations coincide with the relatively reduced ion kinetics as displayed in Fig. 7e, and thus demonstrate that the V_2O_5@PEDOT-50m electrode might encounter a larger ion diffusion resistance than the pristine V_2O_5 nanowires electrode despite the slightly larger specific surface area of V_2O_5@PEDOT-50m (30 m^2 g^{-1}) as compared with the V_2O_5 nanowires (5.7 m^2 g^{-1}).

The structure evolution of V_2O_5@PEDOT-50m at different charge and discharge stages was investigated by *ex situ* XRD (Fig. 8a–c). In the discharging process (Fig. 8b), the diffraction peaks of V_2O_5@PEDOT-50m gradually weaken, while new diffraction peaks at 6.6°, 12.2°, 20.5°, 28.5° and 33.6° gradually occur, which indicate the formation of $Zn_xV_2O_5 \cdot nH_2O$ due to Zn^{2+} and H_2O co-insertion.[28] This observation suggests that V_2O_5 in the V_2O_5@PEDOT-50m undergoes structural evolution and transforms into the layered $Zn_xV_2O_5 \cdot nH_2O$ with the increase of the interlayer spacing from 4.4 to 13.4 Å upon discharging to 0.2 V.[52] In the following charging process (Fig. 8c), Zn^{2+} ions are extracted from the $Zn_xV_2O_5 \cdot nH_2O$ and the characteristic peaks of V_2O_5@PEDOT-50m re-appear at the full charge state of 1.8 V. It is noteworthy that from the second

cycles on, the insertion and extraction of Zn^{2+} and H_2O proceed concurrently in the $Zn_xV_2O_5\cdot nH_2O$ and V_2O_5@PEDOT-50m electrode because the two phases co-exist when discharged to 1.0 V or charged to 1.8 V (Fig. S10†). Moreover, the similar XRD patterns in the discharge and charge processes of the first and second cycles also confirm the highly reversible Zn^{2+} insertion and extraction. The excellent electrochemical reversibility was also probed by *ex situ* XPS. The survey XPS spectrum of the V_2O_5@PEDOT-50m in the first cycle at a discharge state of 0.2 V displays weak Zn 3s (139.9 eV) and sharp Zn Auger (476.2 and 499.8 eV) signals (Fig. 8d). However, these peaks become very weak when fully charged to 1.8 V. Such change means that the markedly reduced binding energy of Zn^{2+} with the V_2O_5@PEDOT host (Fig. 6c) greatly facilitates the extraction of Zn^{2+} ions from the cathode. This contrast is more evident by comparing the Zn 2p XPS spectra of the V_2O_5@PEDOT-50m electrode (Fig. 8e). As compared with the pristine electrode, the Zn 2p peaks at the first cycle are very strong when discharged to 0.2 V and become very weak when charged to 1.8 V, suggesting the reversible Zn^{2+} insertion and extraction process. The insertion/extraction of Zn^{2+} results in the valence change of V in the cathode (Fig. 8f). When discharged to 0.2 V, the intensity of V^{4+} (516.4 eV of V $2p_{3/2}$) significantly increases and V^{3+} (515.4 eV of V $2p_{3/2}$) apparently appears. A quantitative XPS analysis reveals that the proportion of V^{4+} increases up to 57.7% and V^{3+} increases to 12.8%, in contrast to the 16.5% value of V^{4+} in the pristine electrode, and confirms that the reduction of V^{5+} is due to the insertion of Zn^{2+}. In the full charge state of 1.8 V, the XPS results of V return to that of the pristine sample. The above results demonstrate the highly reversible electrochemical Zn^{2+}/H_2O insertion and extraction process into and from the electrode.

3. Conclusion

In summary, we have developed a facile interfacial polymerization strategy to prepare the V_2O_5@PEDOT core-sheath nanowires with the PEDOT sheath thickness varying from 23.0 to 42.9 nm by controlling the polymerization duration. The PEDOT sheaths over the V_2O_5 nanowires are found to enhance the electrode conductivity, improve the electrode stability by protecting V_2O_5 from dissolution, and weaken electrostatic interactions between Zn^{2+} and the V_2O_5 host to boost the electrochemical reversibility. While the V_2O_5@PEDOT nanowires with thicker PEDOT sheaths lower the electrochemical reaction kinetics, the V_2O_5@PEDOT-50m nanowires electrode is still capable of delivering a specific capacity of 293 mA h g^{-1} at 0.1 A g^{-1} and 225 mA h g^{-1} at 1 A g^{-1}, which are superior to 205 mA h g^{-1} and 142 mA h g^{-1} of the pristine V_2O_5 nanowire electrode, respectively. Moreover, about 97.8% and 99% capacity retention over 100 and 2000 cycles at 0.1 and 10 A g^{-1}, respectively, have also been achieved for the V_2O_5@PEDOT-50m electrode. These performances outperform the V_2O_5 nanowires electrode, and demonstrate that the PEDOT sheaths prepared by interfacial polymerization is an effective method to stabilize the V_2O_5 nanowire for zinc ion storage.

4. Experimental section

4.1 Preparation of the V_2O_5 nanowires sponge

The V_2O_5 nanowires were prepared by a hydrothermal synthesis following a recently reported method.[33] Specifically, about 0.364 g of commercial V_2O_5 was dispersed into 30 mL of distilled water, followed by the addition of 5 mL H_2O_2 of 30% under vigorous stirring. After the reaction proceeded at 40 °C for 50 min, a transparent orange solution was obtained. The resultant solution was then transferred to a 50 mL autoclave, and kept in an oven at 200 °C for 2 days. The final product was dispersed in a suitable volume of deionized water, and stirred under ultrasonic treatment to achieve a homogeneous suspension of V_2O_5 nanowires with a concentration of 1 mg mL^{-1}. Then, the obtained suspension of 40 mL was transferred to a PTFE mold with a geometric size of 6 cm × 6 cm, followed by freezing overnight in the refrigerator, and finally freeze-dried for 10 h to obtain the V_2O_5 sponge.

4.2 Preparation of the V_2O_5@PEDOT core–shell nanowires

The V_2O_5@PEDOT core–shell nanowires were fabricated by a vapor-phase polymerization method.[27,32] First, the V_2O_5 sponge was firstly cut into the size of 3 cm × 3 cm × 1 cm. The sponge was then placed in a 500 mL sealed glass reactor containing two beakers of 5 mL and a reaction scaffold (Fig. S1†). In one beaker, about 20 μL concentrated HCl was added to acidify the sponge at 80 °C for 1 h. Afterwards, the EDOT monomer of 20 μL was added into another beaker. The vapor phase polymerization was carried out at the V_2O_4 nanowires/EDOT interfaces at 80 °C for 20–60 min. The resultant products comprising the V_2O_5 nanowire core and conductive PEDOT shell were obtained, which were denoted as V_2O_5@PEDOT-*t* where *t* represents the gas phase polymerization time in minutes.

4.3 Materials characterization

The morphology and microstructures of the samples were characterized by field-emission scanning electron microscopy (FESEM, SU8020) and field-emission transmission electron microscope (TEM, JEM-2800). The crystallographic phases of the samples and *in situ* XRD data were collected using a DX-2700 X-ray diffractometer with Cu Kα radiation of wavelength (λ = 0.154 nm, 40 kV). A Renishaw inVia Raman spectrometer equipped with a 532 nm laser source was also employed for the collection of Raman spectra. X-ray photoelectron spectroscopy (XPS) spectra were collected on an X-ray photoelectron spectrometer (ESCALAB Xi+, Thermo Fisher Scientific) with an Al Kα (1486.6 eV) excitation source. The conductivities of samples were tested by a standard four-probe technique.

4.4 Electrochemical measurements

The electrode was prepared by mixing the active material (70 wt%), conductive carbon (Ketjen black, 20 wt%) and polyvinylidene fluoride (PVDF, 10 wt%). Then, the slurry was coated onto the stainless steel mesh with a mass loading of 2.0 mg cm^{-2}. A CR2032 coin-type cell was assembled with a zinc foil as anode,

2 M aqueous $Zn(CF_3SO_3)_2$ as the electrolyte, and glass fiber as the separator. The cyclic voltammetry (CV) and electrochemical impedance spectroscopy (EIS) were tested on an Autolab electrochemical workstation of PGSTAT 302N (EIS and CV), while the galvanostatic charge and discharge behavior was measured on a multichannel LAND-CT3002A at room temperature. The galvanostatic intermittent titration technique (GITT) was performed on the Land test system at 0.1 A g^{-1} and 15 minutes intervals. The Zn^{2+} diffusion coefficient ($D_{Zn}{}^{2+}$) was achieved from GITT measurement using the following equation:[53,54]

$$D = \frac{4}{\pi\tau}\left(\frac{n_m V_M}{S}\right)^2\left(\frac{\Delta E_s}{\Delta E_t}\right)^2$$

where τ is the duration time of the current pulse, n_m is the amount of active material (mol), V_M is the unit molar volume of the electrode material (cm^3 mol^{-1}), S is the contact area of the electrode and electrolyte, ΔE_s is associated with the change of the steady-state voltage of the corresponding step, and ΔE_t is the variation of the cell voltage.

Author contributions

Ting Yang and Diheng Xin: conceptualization, formal analysis, investigation and writing – original draft; Nan Zhang and Ruibin Jiang: software; Jing Li and Liqin Dang: data curation; methodology; Qi Li and Xuexia He: review & editing; Jie Sun: validation, formal analysis; Xianchi Zhang: validation; Zhibin Lei and Zonghuai Liu: supervision, funding acquisition, project administration.

Conflicts of interest

The authors declare no conflict of interest.

Acknowledgements

This work was supported by the Fundamental Research Funds for the Central Universities (GK202302005), National Natural Science Foundation of China (No. 51772181), Shaanxi Sanqin Scholars Innovation Team, 111 project (B14041) and the Natural Science Basic Research Plan of Shaanxi Province (No. 2019JLP-12).

Notes and references

1 P. Simon and Y. Gogotsi, *Nat. Mater.*, 2020, **19**, 1151–1163.
2 J. Li, J. Fleetwood, W. B. Hawley and W. Kays, *Chem. Rev.*, 2022, **122**, 903–956.
3 X. Zhao, L. Mao, Q. Cheng, F. Liao, G. Yang and L. Chen, *Carbon*, 2022, **186**, 160–170.
4 X. Jia, C. Liu, Z. G. Neale, J. Yang and G. Cao, *Chem. Rev.*, 2020, **120**, 7795–7866.
5 T. Lv, Y. Peng, G. Zhang, S. Jiang, Z. Yang, S. Yang and H. Pang, *Adv. Sci.*, 2023, **10**, 2206907.
6 D. Kundu, B. D. Adams, V. Duffort, S. H. Vajargah and L. F. Nazar, *Nat. Energy*, 2016, **1**, 16119.
7 J. Kim, S. H. Lee, C. Park, H.-S. Kim, J.-H. Park, K. Y. Chung and H. Ahn, *Adv. Funct. Mater.*, 2021, **31**, 2100005.
8 F. Wan and Z. Niu, *Angew. Chem., Int. Ed.*, 2019, **58**, 16358–16367.
9 G. Fang, J. Zhou, A. Pan and S. Liang, *ACS Energy Lett.*, 2018, **3**, 2480–2501.
10 Y. Wang, L. Liu, Y. Wang, J. Qu, Y. Chen and J. Song, *ACS Nano*, 2023, **17**, 21761–21770.
11 W. Jiang, X. Xu, Y. Liu, L. Tan, F. Zhou, Z. Xu and R. Hu, *J. Alloys Compd.*, 2020, **827**, 154273.
12 Y. Xue, Y. Chen, X. Shen, A. Zhong, Z. Ji, J. Cheng, L. Kong and A. Yuan, *J. Colloid Interface Sci.*, 2022, **609**, 297–306.
13 Z. Liu, G. Pulletikurthi and F. Endres, *ACS Appl. Mater. Interfaces*, 2016, **8**, 12158–12164.
14 H. Geng, M. Cheng, B. Wang, Y. Yang, Y. Zhang and C. C. Li, *Adv. Funct. Mater.*, 2020, **30**, 1907684.
15 X. Chen, H. Zhang, J.-H. Liu, Y. Gao, X. Cao, C. Zhan, Y. Wang, S. Wang, S.-L. Chou, S.-X. Dou and D. Cao, *Energy Storage Mater.*, 2022, **50**, 21–46.
16 Y. Lu, T. Zhu, W. van den Bergh, M. Stefik and K. Huang, *Angew. Chem., Int. Ed.*, 2020, **59**, 17004–17011.
17 Y. C. Bai, Y. Qin, J. Y. Hao, H. Zhang and C. M. Li, *Adv. Funct. Mater.*, 2024, 2310393.
18 D. Zhao, X. Wang, W. Zhang, Y. Zhang, Y. Lei, X. Huang, Q. Zhu and J. Liu, *Adv. Funct. Mater.*, 2023, **33**, 2211412.
19 Y. Liu and X. Wu, *J. Energy Chem.*, 2021, **56**, 223–237.
20 D. Selvakumaran, A. Pan, S. Liang and G. Cao, *J. Mater. Chem. A*, 2019, **7**, 18209–18236.
21 M. Song, H. Tan, D. Chao and H. J. Fan, *Adv. Funct. Mater.*, 2018, **28**, 1802564.
22 H. Zhao, Q. Fu, D. Yang, A. Sarapulova, Q. Pang, Y. Meng, L. Wei, H. Ehrenberg, Y. Wei, C. Wang and G. Chen, *ACS Nano*, 2020, **14**, 11809–11820.
23 Y. Jiang, Z. Wu, F. Ye, R. Pang, L. Zhang, Q. Liu, X. Chang, S. Sun, Z. Sun and L. Hu, *Energy Storage Mater.*, 2021, **42**, 286–294.
24 X. Wang, B. Xi, X. Ma, Z. Feng, Y. Jia, J. Feng, Y. Qian and S. Xiong, *Nano Lett.*, 2020, **20**, 2899–2906.
25 M. Yan, P. He, Y. Chen, S. Wang, Q. Wei, K. Zhao, X. Xu, Q. An, Y. Shuang, Y. Shao, K. T. Mueller, L. Mai, J. Liu and J. Yang, *Adv. Mater.*, 2018, **30**, 1703725.
26 Y. Xu, G. Fan, P. X. Sun, Y. Guo, Y. Wang, X. Gu, L. Wu and L. Yu, *Angew. Chem., Int. Ed.*, 2023, **62**, e202303529.
27 W. Bi, Y. Wu, C. Liu, J. Wang, Y. Du, G. Gao, G. Wu and G. Cao, *ACS Appl. Energy Mater.*, 2019, **2**, 668–677.
28 H. Liu, L. Jiang, B. Cao, H. Du, H. Lu, Y. Ma, H. Wang, H. Guo, Q. Huang, B. Xu and S. Guo, *ACS Nano*, 2022, **16**, 14539–14548.
29 F. Wan, S. Huang, H. Cao and Z. Niu, *ACS Nano*, 2020, **14**, 6752–6760.
30 X. Liu, W. Ni, Y. Wang, Y. Liang, B. Wu, G. Xu, X. Wei and L. Yang, *Small*, 2022, **18**, 2105796.
31 X. Ren, D. Ai, R. Lv, F. Kang and Z.-H. Huang, *Electrochim. Acta*, 2020, **336**, 135723.
32 W. Bi, G. Gao, G. Wu, M. Atif, M. S. AlSalhi and G. Cao, *Energy Storage Mater.*, 2021, **40**, 209–218.
33 Y. Guo, Y. Zhang, Y. Zhang, M. Xiang, H. Wu, H. Liu and S. Dou, *J. Mater. Chem. A*, 2018, **6**, 19358–19370.

34 J. Zhou, L. Shan, Z. Wu, X. Guo, G. Fang and S. Liang, *Chem. Commun.*, 2018, **54**, 4457–4460.
35 S. Chen, K. Li, K. S. Hui and J. Zhang, *Adv. Funct. Mater.*, 2020, **30**, 2003890.
36 D. Xu, H. Wang, F. Li, Z. Guan, R. Wang, B. He, Y. Gong and X. Hu, *Adv. Mater. Interfaces*, 2019, **6**, 1801506.
37 D. Zhao, Q. Zhu, X. Li, M. Dun, Y. Wang and X. Huang, *Batteries Supercaps*, 2022, **5**, e202100341.
38 X. Han, J. Sun, Q. Li, X. He, L. Dang, Z. Liu and Z. Lei, *ACS Sus. Chem. Eng.*, 2023, **11**, 2938–2948.
39 X. Zhu, X. Han, R. Guo, P. Yuan, L. Dang, Z. Liu and Z. Lei, *Appl. Surf. Sci.*, 2022, **597**, 153684.
40 M.-Y. Zhang, Y. Song, X. Mu, D. Yang, Z. Qin, D. Guo, X. Sun and X.-X. Liu, *Small*, 2022, **18**, 2107689.
41 P. Hu, T. Zhu, J. Ma, C. Cai, G. Hu, X. Wang, Z. Liu, L. Zhou and L. Mai, *Chem. Commun.*, 2019, **55**, 8486–8489.
42 W. Gao, J. Michalička and M. Pumera, *Small*, 2022, **18**, 2105572.
43 W. Tang, B. Lan, C. Tang, Q. An, L. Chen, W. Zhang, C. Zuo, S. Dong and P. Luo, *ACS Sus. Chem. Eng.*, 2020, **8**, 3681–3688.
44 L. Zhang, I. A. Rodríguez-Pérez, H. Jiang, C. Zhang, D. P. Leonard, Q. Guo, W. Wang, S. Han, L. Wang and X. Ji, *Adv. Funct. Mater.*, 2019, **29**, 1902653.
45 S. Wang, Z. Yuan, X. Zhang, S. Bi, Z. Zhou, J. Tian, Q. Zhang and Z. Niu, *Angew. Chem., Int. Ed.*, 2021, **60**, 7056–7060.
46 X. Wang, B. Xi, Z. Feng, W. Chen, H. Li, Y. Jia, J. Feng, Y. Qian and S. Xiong, *J. Mater. Chem. A*, 2019, **7**, 19130–19139.
47 J. Wang, J. Polleux, J. Lim and B. Dunn, *J. Phys. Chem. C*, 2007, **111**, 14925–14931.
48 R. Guo, P. Yuan, X. Han, X. He, J. Lu, Q. Li, L. Dang, J. Sun, Z. Liu and Z. Lei, *Small*, 2023, **19**, 2205947.
49 H. Sun, F. Niu, P. Yuan, X. He, J. Sun, Z. Liu, Q. Li and Z. Lei, *Small Struct.*, 2021, **2**, 2100029.
50 Y. Li, Z. Huang, P. K. Kalambate, Y. Zhong, Z. Huang, M. Xie, Y. Shen and Y. Huang, *Nano Energy*, 2019, **60**, 752–759.
51 J. Q. Zheng, C. F. Liu, M. Tian, X. X. Jia, E. P. Jahrman, G. T. Seidler, S. Q. Zhang, Y. Y. Liu, Y. F. Zhang, C. G. Meng and G. Z. Cao, *Nano Energy*, 2020, **70**, 104519.
52 N. Zhang, Y. Dong, M. Jia, X. Bian, Y. Wang, M. Qiu, J. Xu, Y. Liu, L. Jiao and F. Cheng, *ACS Energy Lett.*, 2018, **3**, 1366–1372.
53 Y. Zhang, Z. Yu, X. Zhang, X. He, Q. Li, J. Sun, L. Dang, Z. Liu and Z. Lei, *ACS Sus. Chem. Eng.*, 2023, **11**, 14816–14826.
54 S. Li, Y. Liu, X. Zhao, Q. Shen, W. Zhao, Q. Tan, N. Zhang, P. Li, L. Jiao and X. Qu, *Adv. Mater.*, 2021, **33**, 2007480.